Effects of Shearing and Extensional Flows on the Alignment of Colloidal Rods

Macromolecules

pubs.acs.org/Macromolecules Article

Effects of Shearing and Extensional Flows on the Alignment of Colloidal Rods

Vincenzo Calabrese,* Simon J. Haward, and Amy Q. Shen*

Cite This: *Macromolecules* 2021, 54, 4176–4185 Read Online

ACCESS | Metrics & More | Article Recommendations | Supporting Information

ABSTRACT: Cellulose nanocrystals (CNC) can be considered as model colloidal rods and have practical applications in the formation of soft materials with tailored anisotropy. Here, two contrasting microfluidic devices are employed to perform an experimental quantification of the role of shearing and planar extensional flows on the alignment of a dilute CNC dispersion. Characterization of the flow field by microparticle image velocimetry is coupled to flow-induced birefringence analysis to quantify the deformation rate−alignment relationship. The deformation rate required for CNC alignment is 4× smaller in extension than in shear. The birefringence signal rising from the CNC alignment in shear and extension can be scaled on a single master curve using a Péclet number that accounts for the shear and extensional viscosity of the solvent fluid, respectively. Based on this simple scaling relationship, it is possible to anticipate the alignment of rigid colloidal rods under purely extensional deformation by knowing the respective alignment profile in a shearing flow that is more accessible via multiple rheo-optical techniques. Quantification of the differences between shearing and extensional kinematics at aligning colloidal rods establishes coherent guidelines for the manufacture of structured soft materials.

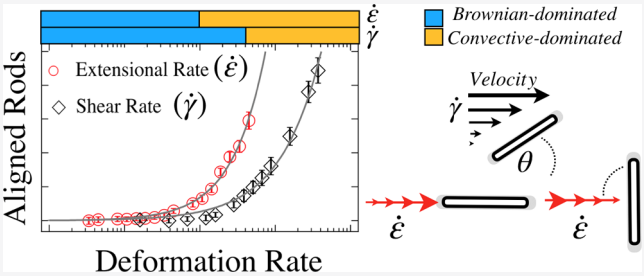

INTRODUCTION

Colloidal rods have received long-lasting attention as building blocks for complex materials because of their effective gelling properties and their ability to orient upon hydrodynamic forces, allowing the manufacture of materials with tailored anisotropy.[1−3] Soft materials with anisotropic orientation have shown a large number of advantages, such as their mechanical strength,[4,5] structural color,[6] electrical and thermal conductivity,[7,8] and directional control of cell growth.[9]

To achieve directionality in soft materials, microfluidic platforms have been extensively used to control hydrodynamic forces, mainly through shearing- and extensional-dominated flows, to aid particle alignment while keeping negligible inertia effects. The relative strength between diffusion and hydrodynamic forces is typically described by the Péclet number $Pe = |E|/Dr$, where $|E|$ is the characteristic deformation rate, and the rotational diffusion coefficient for noninteracting rods, Dr, is described as[10,11]

$$Dr = \frac{3k_B T \ln(l/d_{eff})}{\pi \eta_s l^3} \quad (1)$$

where k_B is the Boltzmann constant, T is the temperature, η_s is the solvent shear viscosity, l is the length, and d_{eff} is the effective diameter of the rod, which accounts for the thickness of the electric double layer. For $Pe < 1$, the particle motion is dominated by Brownian fluctuations, while for $Pe \geq 1$, the particles are perturbed by the flow field. It has been shown, experimentally and theoretically, that shearing flows enable a gradual alignment of anisotropic particles toward the flow direction, where particles align with a preferential angle of 45° at $Pe \simeq 1$ and achieve orientation parallel to the flow direction, 0°, at $Pe \gg 1$.[12−15] Although shear-dominated flows are relatively simple to study *via* conventional rheo-optics techniques, purely extensional flows in conditions where shear forces are negligible are experimentally difficult to assess.[16−18] Consequently, much less is known on how extensional rates affect the orientation of particles in shear-free conditions. Nonetheless, it has been shown that extensional rates enable an additional control on particle orientations, inducing, for instance, particle alignment perpendicular to the flow direction, which is not possible in shearing flows.[7,19−21] Of considerable importance is the work of Corona et al., who investigated the effects of shearing- and extension-dominated flows on the alignment of a concentrated suspension of colloidal rods using a fluidic four-roll mill device.[22] However, no significant differences could be discerned between shearing- and extensional-dominated flows

Received: September 17, 2020
Revised: January 21, 2021
Published: February 4, 2021

https://dx.doi.org/10.1021/acs.macromol.0c02155
Macromolecules 2021, 54, 4176−4185

as excluded volume effects were likely dominant at the high concentration tested. Recent work from Rosén et al.[23] elucidated that for extension-dominated flows, generated in flow-focusing and converging channels, a reduced rotational diffusion coefficient was obtained compared to shearing flows. Nonetheless, difficulties rising from interparticle interactions, particle flexibility, and a nonuniform extensional rate within the microfluidic channel hindered a comprehensive quantitative examination to decouple the effects of shearing- and extensional-dominated flows. In addition, for mixed flows comprising shearing and extensional kinematics, Trebbin et al. determined the relative strength of extensional vs shear forces required to induce the alignment of rodlike particles perpendicular to the flow direction in an expansion-flow geometry.[19] However, to date, an experimental comparison between shear and extensional rate-driven alignment of rodlike particles in shearing and purely extensional flows under conditions of negligible interparticle interactions (dilute regime) is still missing. In this article, we couple quantitative flow field measurements with state-of-the-art flow-induced birefringence (FIB) analysis to elucidate, experimentally, the role of shear and extensional rates at aligning a dilute colloidal suspension of rodlike particles in the limit of small deformation rates ($0.1 \lesssim Pe \lesssim 10$). The experiments are conducted using a dilute cellulose nanocrystal (CNC) suspension consisting of noninteracting negatively charged rigid rodlike nanoparticles.[24]

MATERIALS AND METHODS

Test Fluid. The CNC was purchased from CelluForce (Montreal, Canada) as an aqueous 5.6 wt % stock dispersion at pH 6.3. The majority of the experiments were performed using a 0.1 wt % CNC dispersion prepared by dilution of the stock dispersion with deionized water and used without further treatment. Where specified, a 0.1 wt % CNC was prepared in a Newtonian solvent composed of a glycerol:water mixture containing 17.2 vol % glycerol (Sigma-Aldrich 99%, η_s = 1.6 mPa·s).[25] The CNC concentration is chosen to be sufficiently large to obtain values of birefringence significantly above the detection limit of our imaging system (described below), yet below the onset of interparticle interactions and below the critical concentration required to form cholesteric tactoids (≈0.5 wt %) so the CNC is isotropically distributed in the bulk phase.[26] Extensive characterization of CNC from the same industrial producer is described by Bertsch et al.[26,27] and Reid et al.[28]

Shear Rheometry. Steady shear rheology of the 0.1 wt % CNC dispersion was measured using a strain-controlled ARES-G2 rotational shear rheometer (TA Instruments, Inc.) equipped with a double-gap geometry (with an inner and outer gap of 0.81 and 1.00 mm, respectively) composed of a stainless steel bob and a hard-anodized aluminum cup. The dispersion was covered with a solvent trap and measurements were performed at 25 °C (controlled by an advanced Peltier system with a temperature accuracy of ± 0.1 °C) over a range of shear rate, $20 \leq \dot{\gamma} \leq 300$ s^{-1}. A microfluidic slit rheometer (m-VROC RheoSense, Inc.), equipped with an A10 pressure cell, 3 mm wide and 100 μm high, was used to access the rheological response of the test fluid at high values of shear rate (up to $\dot{\gamma} \approx 3 \times 10^4$ s^{-1}). The experiment was carried out at 25 °C (controlled via an external circulating water bath with a temperature accuracy of ± 0.1 °C).

Atomic Force Microscopy (AFM). A 0.01 wt % CNC dispersion was drop-cast on a mica substrate and imaged using an atomic force microscope (Dimension ICON3, Bruker) in tapping mode. The distribution of the particle contour length, l, and diameter, d, was extrapolated by tracking 976 isolated particles using an open-source code, FiberApp.[29] The value of d was obtained from the AFM height profile.

Microfluidic Platforms. A shearing flow-dominated channel (SFC) and an optimized shape cross-slot extensional rheometer (OSCER)[16,30] were used to generate two-dimensional (2D) flows that, in discrete areas of the geometries, provide good approximations to purely shearing and purely extensional flows, respectively (Figure 1). The SFC consists of a straight channel of fused silica glass with a rectangular cross section (length L = 25 mm along the x-axis, height H = 2 mm along the z-axis, and width W = 0.4 mm along the y-axis, resulting in an aspect ratio $\alpha = H/W = 5$), fabricated with a selective laser-induced etching (SLE) technique[31,32] (Figure 1a). The OSCER is based on a planar cross-slot geometry with two incoming and outgoing flows placed orthogonal to each other, as described by Haward et al.[16,30] and depicted in Figure 1b. The device has a height of H = 2.1 mm along the z-axis and a channel width of W = 0.2 mm at the inlets and outlets, yielding α = 10.5, generating a good approximation of a 2D flow field which is extensional-dominated and shear-free in a large region around the stagnation point, at $x = y = 0$ (see the coordinate system in Figure 1b). The fluid elements are compressed along the y-axis and extended along the x-axis (referred to as the compression and elongation axes, respectively; Figure 1b).

The flow inside the channels is driven by Nemesys low-pressure syringe pumps (Cetoni, GmbH) and Hamilton Gastight syringes, which infuse the liquid at the inlet and withdraw it at an equal and opposite volumetric rate, Q (m^3 s^{-1}), from the outlet. To ensure steady flows, the highest flow rates were set at Reynolds numbers, $Re = \rho UW/\eta$, of 15.4 and 6.4, for the SFC and OSCER, respectively, considering a fluid density, ρ = 1000 kg m^{-3}, an average flow velocity as $U = Q/HW$ (m s^{-1}) and a CNC suspension shear viscosity η = 1.3 mPa·s as determined by rheological measurements (detailed in the following section). The flows were equilibrated for at least 5 s before all measurements and confirmed as being steady by inspection of the microparticle image velocimetry (μ-PIV; see next section) flow fields prior to their time averaging. All of the experiments were carried out at the ambient laboratory temperature (25 ± 1 °C).

Micro-Particle Image Velocimetry (μ-PIV). The flow fields in the SFC and OSCER devices were obtained using time-averaged μ-PIV of the test fluid seeded with 1.1 μm fluorescent particles (FluoroMax, Thermo Fisher), to a concentration of ≈0.02 wt %. The μ-PIV measurements were conducted using a volume illumination system (TSI Inc., MN) installed on an inverted microscope (Nikon Eclipse Ti). Nikon PlanFluor objective lenses of 4× and 10× with numerical apertures of NA = 0.13 and 0.30 were used for the OSCER and SFC device, respectively. Each geometry was placed with the z-axis parallel to the light source and for all of the flow rates tested, a sequence of at least 100 image pairs were acquired at the midplane of the geometries

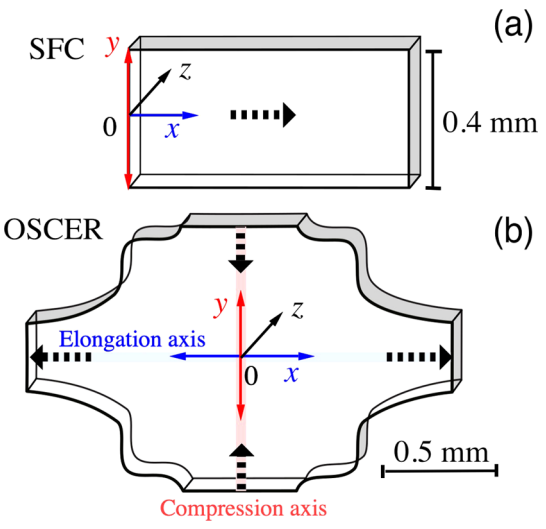

Figure 1. Schematic diagrams of (a) the shearing flow-dominated channel (SFC) and (b) the optimized shape cross-slot extensional rheometer (OSCER) with respective coordinate system and scale bar. The dashed arrows indicate the flow direction.

https://dx.doi.org/10.1021/acs.macromol.0c02155
Macromolecules 2021, 54, 4176−4185

(z = 1 mm). For the SFC, images were acquired at a distance of ≈$L/2$ from the inlet to ensure fully developed velocity profiles. The average displacement of the seeded particles between the two images in each pair was kept constant at ≈4 pixels. The measurement depths, δz_m, corresponding to the depth over which the seeded particles contribute to the determination of the velocity field was δz_m = 150 and 35 μm, for the OSCER and SFC, respectively.[33] Cross-correlation between image pairs provided velocity vectors on a square grid with a spacing of 32 × 32 and 12.8 × 12.8 μm for the OSCER and SFC, respectively. Data analysis was performed using a custom-made Matlab routine.

Flow-Induced Birefringence (FIB). Flow-induced birefringence (FIB) measurements were performed using an Exicor MicroImager (Hinds Instruments Inc.). Monochromatic light of wavelength λ = 450 nm was shone through a linear polarizer at 0°, a photoelastic modulator (PEM) at 45°, the SFC or the OSCER containing the testing fluid, a PEM at 0°, and a linear polarizer at 45°, in the order given. The geometries were imaged using a 5× objective in the same position as described for μ-PIV. The instrument performs Mueller matrix decomposition, determining the elements of 4 × 4 Mueller matrices using a stroboscopic light source. The retardance R, describing the total phase shift occurring between the two orthogonally polarized light beams, and the orientation of the slow optical axis (extraordinary ray), θ, were obtained from a total of seven images acquired at 1 frame/s. The retardance, R (measured in nm), was then converted to birefringence as $\Delta n = R/H$. The background value of Δn was determined for the test fluid at rest and subtracted for all of the analyses presented. The background value determined in both geometries was $\Delta n \approx 6 \times 10^{-7}$ and comparable to the instrument resolution of $\Delta n \approx 3 \times 10^{-7}$. Quantitative analysis of θ was restricted to values of $\Delta n \gtrsim 3 \times 10^{-6}$, corresponding to 10× the instrument resolution. The spatial resolution of the measurement was ≈2 μm/pixel and data analysis was performed using a custom-made Matlab routine.

RESULTS AND DISCUSSION

Characterization of the Test Fluid. We begin by estimating the number density, $\nu = N/V$, of the 0.1 wt % CNC dispersion, where N is the number of rods and V is the sample volume. In suspensions of monodisperse rodlike particles, the number density, ν, is commonly used to distinguish between the dilute, semidilute, and concentrated regimes.[1] For monodisperse rods, the calculation of ν is straightforward as a single particle length (l) and diameter (d) are sufficient to describe the whole particle population. Contrarily, for a polydisperse distribution of rods such as CNC, the large span of lengths must be considered for a more accurate estimation of ν. Thus, the size distribution of the CNC was extrapolated from atomic force microscopy (AFM) images (Figure 2a,b). The average contour length was $\langle l \rangle$ = 260 ± 180 nm and the average diameter $\langle d \rangle$ = 4.8 ± 1.8 nm. The effective number density, ν_e, was thereafter estimated as

$$\nu_e = \frac{N_e}{V} = \frac{\sum_{i=1}^{l_{max}} \left(\frac{V_{CNC}\phi_i}{V \mathrm{cyl}_i} \right)}{V} \quad (2)$$

where N_e is the effective number of rods, l_{max} is the longest detected contour length (700 nm), V_{CNC} is the volume of the CNC in the sample (which can be estimated using a density of 1500 kg m^{-3}),[34] ϕ_i is the volume fraction of the rods with length i, and V cyl$_i$ is the volume occupied by a single rod with length i, for which a cylindrical morphology can be approximated. It is noted that the distribution of the CNC diameters, d, is not accounted for in eq 2 since it has only a minimal effect on the estimation of ν_e of slender objects and $\langle d \rangle$ is used to obtain V cyl$_i$. For the 0.1 wt % CNC, $\nu_e \approx 1/\langle l \rangle^3$, indicating that at this concentration, the CNC dispersion is at the onset of the semidilute regime, where the particles rarely interact (although more frequently than in the dilute regime).[11,35] The absence of pronounced interparticle interactions was reported by Bertsch et al. for concentrations below 0.5 wt %, as shown by small-angle X-ray scattering (SAXS) studies of CNC from the same source as that used in the present work.[26] In addition, from the AFM images, a persistence length, $l_p \approx 30\langle l \rangle$ was extrapolated using the method of the mean-square midpoint displacement (MSMD) within the FiberApp routine and detailed by Usov and Mezzenga,[29] indicating that CNC can be well described as

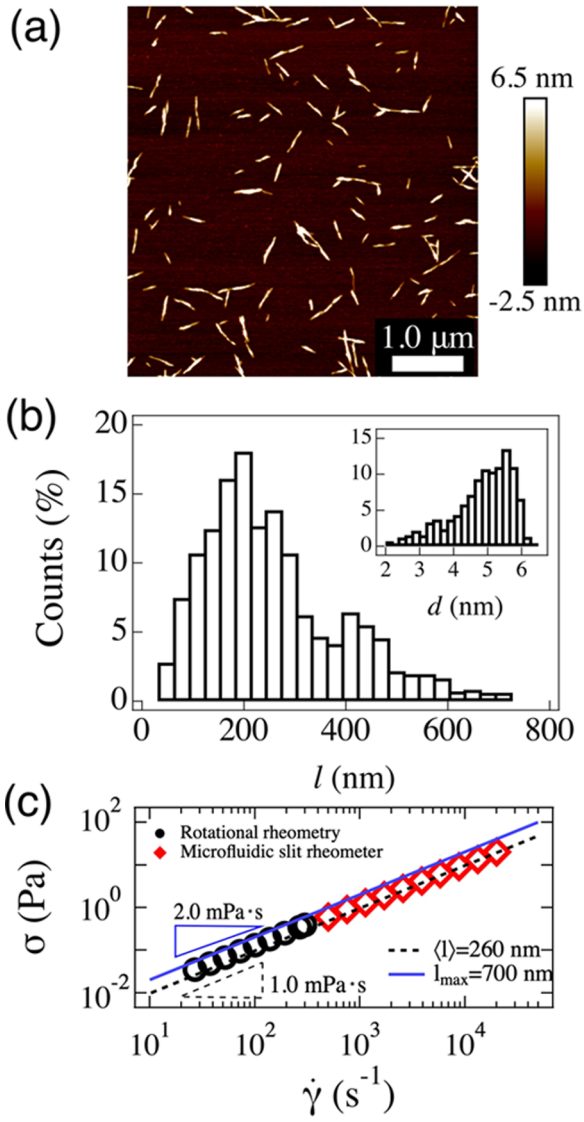

Figure 2. (a) Tapping-mode atomic force microscopy (AFM) image of a drop-cast 0.01 wt % CNC dispersion on mica substrate. (b) Particle contour length, l, and particle diameter, d (inset in (b)), distributions as obtained from the AFM counting of 976 isolated particles. (c) Flow curve of the 0.1 wt % CNC dispersion presented as shear stress σ vs shear rate $\dot{\gamma}$. The black circles are data obtained using a rotational strain-controlled rheometer (ARES-G2). The data represented by the diamonds are obtained using a microfluidic slit rheometer (m-VROC). The dashed (black) and solid (blue) lines are the predictions of the zero shear viscosity from eq 4 using values of average length, $\langle l \rangle$, and maximum length, l_{max}, respectively, as obtained from AFM analysis.

https://dx.doi.org/10.1021/acs.macromol.0c02155
Macromolecules 2021, 54, 4176−4185

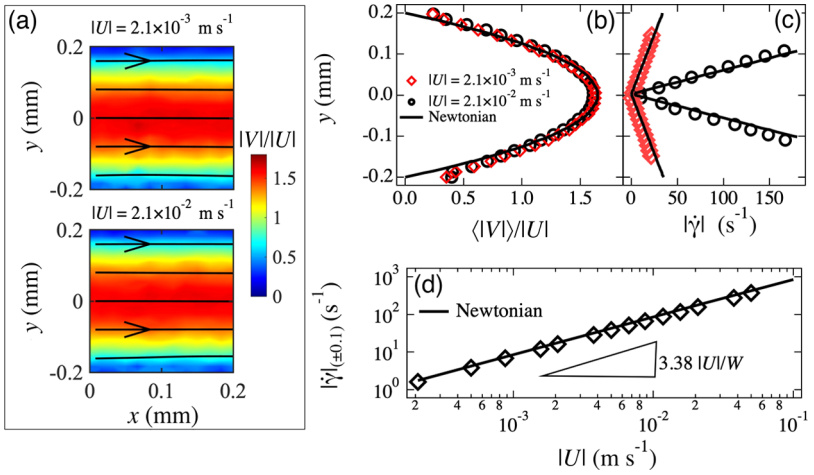

Figure 3. (a) Time-averaged results of flow velocimetry (μ-PIV) with superimposed streamlines for the SFC containing the 0.1 wt % CNC dispersion. Two representative average flow velocities, $|U|$, are displayed. (b) Normalized spatially averaged velocity profiles taken across the y-axis of the channel, for values of $|U|$ as in (a). (c) Magnitude of shear rate, $|\dot{\gamma}| = \partial|V_x|/\partial|y|$, as obtained from the velocity profile displayed in (b). (d) Magnitude of the shear rate obtained from the average of $|\dot{\gamma}|$ at $y = \pm 0.1$ mm, $|\dot{\gamma}|_{(\pm 0.1)}$, as a function of the average flow velocity. In (b–d), the solid lines are the infinite series analytical solution for creeping Newtonian flow.[42]

rigid rods. A value of $l_p \gg l$ was also obtained when l_p was calculated as[36]

$$l_p = \frac{\pi \langle d \rangle^4 G}{64 k_B T} \tag{3}$$

using the reported values of the CNC elastic modulus, G, between 5 and 150 GPa.[34]

The steady shear rheology of the 0.1 wt % CNC dispersion is shown in Figure 2c. The shear stress, σ, of the 0.1 wt % CNC suspension followed a linear relationship with the shear rate, $\dot{\gamma}$, as for a Newtonian fluid with shear viscosity η = 1.3 mPa·s. The Newtonian-like behavior is explained by the low concentration of CNC in the suspension, which hinders any experimental evaluation of the shear-thinning behavior expected for anisotropic particles in the shearing flow.[35,37−41]

From eq 1, it is clear that longer rods will align at lower shear rates than shorter rods since $Dr \propto 1/l^3$. As such, in polydisperse suspensions of noninteracting colloidal rods, the onset of shear-thinning is dictated by the longest population of rods. Substituting l with l_{max} and accounting for the contribution of the electric double layer (δd = 22.6 nm)[26] to the effective diameter ($d_{eff} \approx \delta d + \langle d \rangle$) in eq 1, we estimated the expected onset of the shear-thinning at $\dot{\gamma} \simeq 40\ s^{-1}$ ($Pe \simeq 1$). For a dilute suspension of monodisperse rods, neglecting interparticle interactions, the zero shear viscosity, η_0, can be estimated from the Doi−Edwards theory,[10,11] given by Lang et al.[35] as

$$\eta_0 \simeq \eta_s + \nu_e k_B T \left(\frac{1}{30} \frac{1}{Dr} \right) \tag{4}$$

When the value of l in eq 1 is substituted with either $\langle l \rangle$ or l_{max}, the predicted values of the zero shear viscosity fully envelop the experimental data (Figure 2c). The lack of any further contribution needed to account for interparticle interactions in eq 4, suggests, in agreement with Bertsch et al.,[26] that the 0.1 wt % CNC suspension can be considered in the dilute noninteracting regime.

Flow Profiles. The bulk rheometry gives a good indication that the dilute CNC dispersion behaves as a Newtonian fluid. Consequently, no information regarding the onset of alignment, as usually associated with the onset of shear-thinning, can be discerned from the flow curve. To define a deformation rate−alignment relationship of the dilute CNC dispersion we focus on the control of the shear rate, $\dot{\gamma}$, and extensional rate, $\dot{\epsilon}$ in two separate microchannels. The SFC was used to provide a well approximated 2D shearing flow. Figure 3a shows two representative time-averaged flow fields obtained by μ-PIV at the midplane (z = 1 mm) of the SFC. The velocity magnitude $|V|$, as measured by μ-PIV, is scaled by the average flow velocity $|U|$. The flow field displays a velocity gradient across the channel width (y-axis) with the greater velocity along the centerline. This is evident when plotting the spatially averaged velocity, namely, $\langle |V| \rangle$ (determined by averaging $|V|$ along 0.2 mm of the x-axis) as $\langle |V| \rangle / |U|$ vs the channel width (y-axis), where a parabolic (Poiseuille) flow profile is displayed (Figure 3b). The measured flow profile is in quantitative agreement with an infinite series analytical solution for creeping Newtonian flow[42] as depicted by the solid line in Figure 3b, consistent with the Newtonian-like behavior described by the rheological measurement in Figure 2. From the velocity profile displayed in Figure 3b, we compute the shear rate profile as $|\dot{\gamma}| = \partial|V_x|/\partial|y|$, where $|V_x|$ is the x-component of velocity (Figure 3c).

The magnitude of the shear rate is also in good agreement with the expectation for a Newtonian fluid (black lines). Since the shear rate varies substantially along the channel y-axis, we select the value of the shear rate at the location $y = \pm 0.1$ mm, namely, $|\dot{\gamma}|_{(\pm 0.1)}$ (computed as the average of the $|\dot{\gamma}|$ at y = 0.1 and −0.1 mm), which is the midpoint in $|y|$ between the minimum and the maximum value of $|\dot{\gamma}|$. The location $y = \pm 0.1$ mm is also far from the channel side walls, where the μ-PIV limitations become evident, while still providing relatively high values of shear rate. The relation between $|\dot{\gamma}|_{(\pm 0.1)}$ and the average velocity $|U|$ can therefore be established as shown in Figure 3d, leading to $|\dot{\gamma}|_{(\pm 0.1)} = 3.38|U|/W$, which satisfies the expectation for a Newtonian fluid (solid line).

The OSCER is used to generate a 2D flow field with an extensional-dominated flow in a large region around the stagnation point (the point of zero velocity at $x = y = 0$, Figure

https://dx.doi.org/10.1021/acs.macromol.0c02155
Macromolecules 2021, 54, 4176−4185

1b).[16,30,43] The two incoming and outgoing flows are orthogonal to each other and indicated by the dashed arrows in Figure 4a. The μ-PIV profiles for two characteristic average velocities, $|U|$, display a symmetric and Newtonian-like behavior of the CNC suspension (Figure 4a). The x-component of velocity, V_x, obtained along the elongation axis (at $y = 0$) increases linearly with x (Figure 4b) and, analogously, the y-component of velocity, V_y (at $x = 0$) along the compression axis, decreases linearly with y (Figure 4c). This indicates uniform extensional rates along both the compression and elongation axes and therefore Newtonian-like behavior in planar extension. As such, the values of compression and elongation rates can be directly obtained from the slope of the plots in Figure 4b,c. In Figure 4d, the magnitude of the compression and elongation rate as a function of the average flow velocity $|U|$ collapsed on a single curve, indicating that the extensional rates, $\dot{\varepsilon}$, along the compression and extension axes are equal and opposite, as for an ideal planar extension.[30] The $|\dot{\varepsilon}|$ followed a linear relationship with $|U|$ as $|\dot{\varepsilon}| = 0.21|U|/W$, in good agreement with previously reported Newtonian fluids (solid line).[16,30] Note that nonlinear effects such as the increase in extensional viscosity seen in polymer solutions manifest as a deviation from the linear relationship between $|\dot{\varepsilon}|$ and $|U|$.[30,44] This linear behavior suggests that the dilute CNC dispersion behaves as a Newtonian fluid also in extension, giving a CNC suspension extensional viscosity $\eta_E = Tr\,\eta$, where η is the CNC suspension shear viscosity obtained from the shear rheometry measurements displayed in Figure 2c and Tr is the Trouton ratio. It is noted that the value of Tr depends on the type of applied deformation. For Newtonian fluids in uniaxial, biaxial, and planar extensions, Tr = 3, 6, and 4, respectively.[43,45−48] Although experimental reports of the Trouton ratio for Newtonian fluids are limited due to experimental difficulties, especially for low viscosity fluids, Trouton himself experimentally confirmed the value of Tr = 3 in a uniaxial extensional flow by careful measurements using small deformation rates and very viscous fluids.[45,47] The validity of the Trouton ratio is widely accepted due to its consistency with Newton's viscosity law.[45−47] As the OSCER device generates planar extension, we consider Tr = 4, thus $\eta_E = 4\eta$.

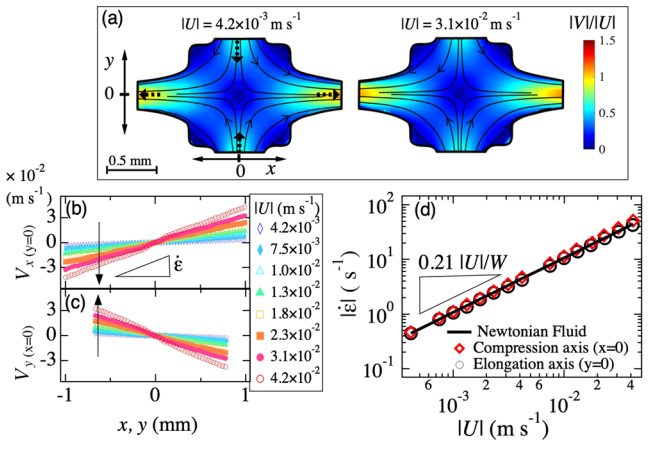

Figure 4. (a) Time-averaged results of flow velocimetry (μ-PIV) with superimposed streamlines for the OSCER containing the 0.1 wt % CNC dispersion. Two representative average flow velocities, $|U|$, are displayed. (b) Velocity component along the elongation axis, V_x, at y = 0 mm. (c) Velocity component along the compression axis, V_y, at x = 0 mm. (d) Magnitude of the extension rate, $|\dot{\varepsilon}|$, as obtained along the compression and elongation axes. The solid line is the expected relationship for a Newtonian fluid.[30]

Flow-Induced Alignment. Since the spatially resolved deformation rates, $|\dot{\gamma}|$ and $|\dot{\varepsilon}|$, have been established, we shift our attention to the impact that the two different deformation rates have on the structural orientation of the dilute CNC dispersion. The contour plots in Figure 5a display the FIB fields in the SFC at two different values of $|U|$. The birefringence intensity, Δn, is displayed by the contour plot and describes the extent of anisotropy in the system. The orientation of the slow optical axis, θ, is displayed by the superimposed solid segments, which directly probe the CNC orientation angle.[12,49] As a metric of comparison, it has been recently shown that both Δn and θ yield excellent agreement with parameters describing the extent of alignment and favorable orientation extrapolated from small-angle X-ray scattering (SAXS) of anisotropic particles, enabling a trustworthy comparison of the FIB with the rheo-small-angle scattering (SAS) literature.[50] The FIB fields in the SFC display the minimum Δn at $y = 0$ (where $\dot{\gamma} = 0\ s^{-1}$) and increase toward the channel walls (Figure 5a). Note that we attribute the narrow region of low FIB signal very close to the walls to "shadowing" by the wall, i.e., due to a slight imprecision of the orthogonal alignment of the microfluidic device on the imaging system (see Figure S1 for Δn profiles across the channel width). Since Δn scales with the volume fraction of aligned particles ($\phi_{aligned}$), it is clear that a greater number of CNC become aligned as the shear rate is increased. Moreover, the CNC orientation, displayed by the solid segments in Figure 5a, shows an overall alignment of the particles toward the flow direction.

In the OSCER device, a large region around the stagnation point displays a strong Δn signal, as clearly visible for the larger value of $|U|$ in Figure 5b (displayed by the light blue color in the contour plot). The direction of the CNC alignment along the compression axis is perpendicular to the flow direction (y-axis) due to the deceleration of the fluid element upon approaching the stagnation point and the consequent negative extensional rate along the y-axis. Contrarily, the CNC aligns parallel to the flow (x-axis) along the elongation axis due to the positive extension rate. Similar orientation trends have been reported for suspensions of anisotropic particles in extensional-dominated flows (in contraction/expansion, cross-slots, and fluidic four-roll mill devices), although in conditions where interparticle interactions play a crucial role on particle alignment.[7,19−21]

To have a good quantitative description of the deformation rate−alignment relationship, we plot the spatially resolved values of Δn as a function of the relevant deformation rate previously determined in the specific locations of the SFC and OSCER geometries (Figure 5c). For the SFC, the spatially averaged birefringence signal, $\langle \Delta n \rangle$, is obtained at $y = \pm 0.1$ mm by averaging Δn along 1 mm in the x-direction, while for the OSCER device, $\langle \Delta n \rangle$ is obtained by averaging Δn along 1 mm of the elongation axis (at $y = 0$ over $-0.5 \le x \le 0.5$ mm; see Figures S1 and S2 for the spatially resolved Δn profiles). The curves shown in Figure 5c for the SFC and the OSCER device display a similar increase in $\langle \Delta n \rangle$ with the deformation rate, $|E|$, which is well calculated by a power law trend as $\langle \Delta n \rangle \propto |E|^p$, where the power law exponent $p = 0.9$. Importantly, the FIB technique enables quantification of the CNC alignment with the deformation rate, which is not

https://dx.doi.org/10.1021/acs.macromol.0c02155
Macromolecules 2021, 54, 4176−4185

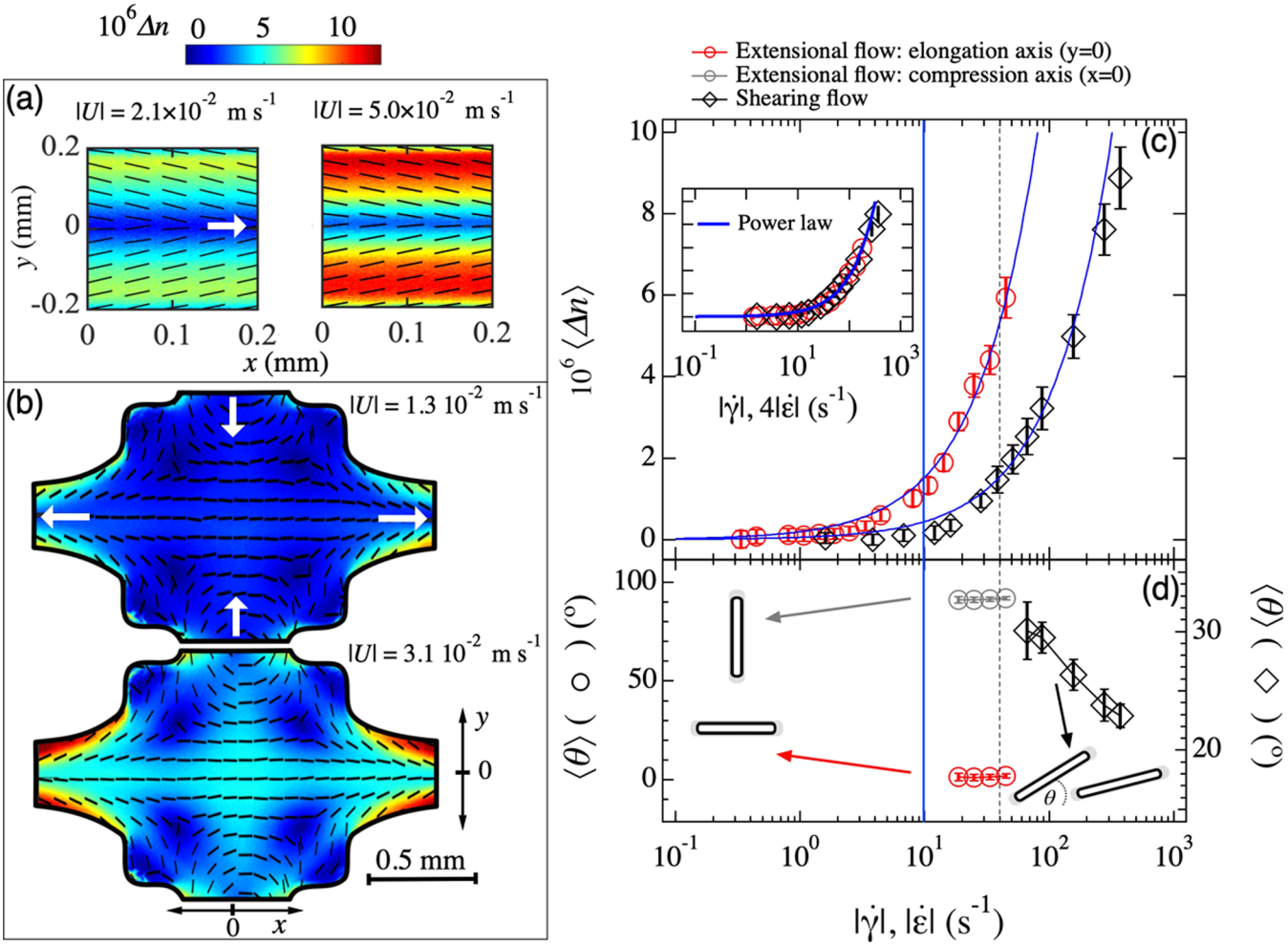

Figure 5. Time-averaged FIB profiles of a 0.1 wt % CNC dispersion, for the (a) SFC and (b) OSCER device. The birefringence, $\langle\Delta n\rangle$, is displayed by the contour plot while the direction of the slow optical axis, θ, is indicated by the solid segments. (c) Spatially averaged birefringence, $\langle\Delta n\rangle$, and (d) spatially averaged orientation angle, $\langle\theta\rangle$, as a function of the magnitude of shear rate, $|\dot\gamma|$, and extension rate $|\dot\varepsilon|$. The $\langle\Delta n\rangle$ and $\langle\theta\rangle$ values are obtained in the same channel location as for the relevant deformation rate. The inset in (c) displays the plot as in (c) with a rescaled x-axis as $4|\dot\varepsilon|$. The solid lines in (c) are power law trends as $\langle\Delta n\rangle \propto |\dot\gamma|^{0.9} \propto |4\dot\varepsilon|^{0.9}$. The dashed (black) and solid (blue) vertical lines are the values of Dr and Dr_E (s^{-1}) estimated *via* eqs 1 and 5, respectively, using $l = l_{max}$.

possible by rheological measurements alone (see Figure 2c). It is noted that for a given applied $|U|$ (hence $\dot\gamma$ profile, Figure 3c), this empirical power law is able to describe the $\langle\Delta n\rangle$ profile across most of the SFC width with reasonable accuracy (see Figure S1 for spatially resolved Δn profiles with the predictions of the empirical power law fitting). From Figure 5c, it is apparent that lower extensional rates are required to induce rod alignment in the OSCER device, than the shear rates required to induce alignment in the SFC. This appears to indicate that extensional forces are more effective at inducing CNC alignment. The $\langle\Delta n\rangle$ profiles obtained for the extensional and shearing flow collapsed on a single master curve when scaling the extensional rate as $4|\dot\varepsilon|$ (inset in Figure 5c). Notably, both curves are well described by the same power law curve with exponent $p = 0.9$. This indicates that extensional and shear forces have a similar relationship with $\phi_{aligned}$ and that the extensional forces are 4 times more effective for the alignment of anisotropic particles compared to shear forces. Therefore, for a Newtonian fluid containing noninteracting rods, the following proportionality can be proposed $\langle\Delta n\rangle \propto |\dot\gamma|^{0.9} \propto |4\dot\varepsilon|^{0.9} \propto \phi_{aligned}$. It is noted that the proportionality factor of 4 corresponds exactly to the value of Tr for Newtonian fluids in planar elongation flows, which sets the relationship between the solvent shear viscosity, η_s, and the solvent extensional viscosity, $\eta_{s,E} = 4\eta_s$.[43] As our purpose is to experimentally test the formal identity of $\langle\Delta n\rangle$ under shear and planar extensional flow, we introduce an extensional rotational diffusion coefficient, Dr_E, which considers the scaling shown in Figure 5c (inset). The use of Dr_E is motivated by the effective conversion of the extent of CNC alignment under shear and planar extension as detailed in the following subsection. Assuming a dominant extensional viscosity of the solvent fluid $\eta_{s,E}$ along the extensional axis, it is plausible to substitute η_s with $\eta_{s,E} = Tr\eta_s$ in eq 1, yielding

$$Dr_E = \frac{3k_BT\ln(l/d_{eff})}{\pi(Tr\eta_s)l^3} = \frac{Dr}{Tr} \quad (5)$$

This explains the superimposing plots in Figure 5c when a scaling of $4|\dot\varepsilon|$ is adopted (see inset). As such, using a shear-free extensional flow and a particle concentration that avoids interparticle interactions clarifies the pivotal role of the solvent viscosity on the volume fraction of aligned particles, $\phi_{aligned}$. Although not validated, the consideration of η_s or $\eta_{s,E}$ for a

https://dx.doi.org/10.1021/acs.macromol.0c02155
Macromolecules 2021, 54, 4176−4185

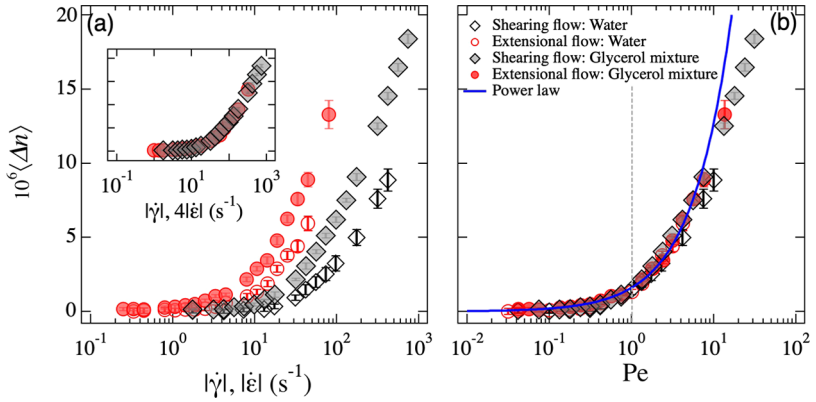

Figure 6. Spatially averaged birefringence, $\langle\Delta n\rangle$, of an aqueous 0.1 wt % CNC dispersion (open symbols) and a 0.1 wt % CNC dispersion in an aqueous glycerol mixture containing 17.2 vol % glycerol (close symbols). (a) $\langle\Delta n\rangle$ as a function of the magnitude of shear rate, $|\dot{\gamma}|$, and extension rate, $|\dot{\varepsilon}|$. The inset in (a) displays the plot as in (a) with a rescaled x-axis as $4|\dot{\varepsilon}|$ for the glycerol mixture as solvent fluid of the CNC. The plot in (a) is rescaled by the Péclet number, Pe, in (b) using the Dr and Dr_E as the scaling diffusion coefficient for the shearing and extensional flow, respectively. The Dr and Dr_E were estimated using eqs 1 and 5, respectively, using $l = l_{max}$.

rotational diffusion coefficient that accounts for shearing- and extensional-dominated flows, respectively, has been previously proposed by Qazi et al.[20] A decreased rotational diffusion coefficient in extensional-dominated flows has also been demonstrated by Rosén et al.[23] for interacting cellulose nanofibrils. However, the absence of interparticle interactions and the uniform, shear-free, elongational flow presented in this work enables the first quantitative elucidation of differences between the rotational dynamics of colloidal rods in shearing and planar extensional flows. However, it must be noted that the dynamics of CNC alignment depends on the type of extensional flow used (i.e., uniaxial, biaxial, and planar), as supported by Singh and Rey[51] via computer simulation studies of discotic liquid crystals. Considering that the longest CNC population (l_{max}) aligns at lower deformation rates, the predicted onset of alignment based on Dr (dashed, black, lines in Figure 5c,d) and Dr_E (solid, blue, lines in Figure 5c,d) do not exactly match the onset of birefringence. This slight deviation is likely caused by the simplified treatment of the CNC as rigid cylindrical rods in eq 1, disregarding surface roughness and the deviations from a perfect cylindrical shape (see Figure S3 for an AFM image of the CNC at the nanometer length scale). However, the scaling factor between the curves in Figure 5c strongly suggests that the larger value of $\eta_{s,E}$ compared to η_s is the cause of the earlier onset of alignment.

To better assess the onset of alignment in shear and extensional flow, we further evaluate quantitatively the CNC orientation as determined by the angle of orientation, θ, with respect to the flow direction (Figure 5d). For the SFC, the spatially averaged angle of the slow optical axis, $\langle\theta\rangle$, was determined in the same location as for the $\langle\Delta n\rangle$, i.e., averaging $|\theta|$ along 1 mm in the x-direction at $y = \pm 0.1$ mm, while for the OSCER device, the $\langle\theta\rangle$ was obtained from averaging θ along 1 mm of the elongation axis at $y = 0$ (averaging θ over $-0.5 \leq x \leq 0.5$ mm) and compression axis at $x = 0$ (averaging θ over $-0.5 \leq y \leq 0.5$ mm; see Figure S2 for θ profiles along the extensional axes). For $|\dot{\gamma}| \gtrsim 10^2$ s^{-1}, $\langle\theta\rangle$ progressively decreases to values of around 22° at the highest shear rates, in good agreement with SAXS and birefringence studies of a dilute CNC suspension.[50] Considering the trend of $\langle\Delta n\rangle$ and $\langle\theta\rangle$ as a function of $|\dot{\gamma}|$, it is possible to discern a Brownian-dominated regime for $|\dot{\gamma}| < 40$ s^{-1}, where the system is isotropic ($\langle\Delta n\rangle \approx 0$), and a convection-dominated regime at $|\dot{\gamma}| \gtrsim 40$ s^{-1}, where the hydrodynamic forces orient the particles toward the flow direction while causing a pronounced increase in $\langle\Delta n\rangle$. Particles in shear flow have the tendency to tumble; thus, it is instructive to compare the rotational diffusion time $t_d = 1/Dr$ with the Jeffery oscillation period $\tau_j = 2\pi(Ar + Ar^{-1})/\dot{\gamma}$.[12,52,53] Following Zöttl et al., we introduce a Péclet number that measures the persistence of tumbling events, herein referred to as the Jeffery–Péclet number $Pe_j = t_d/\tau_j$, where for $Pe_j \gtrsim 1$, particles undergo deterministic tumbling. A representative particle aspect ratio $Ar = l_{max}/d_{eff}$ and $\dot{\gamma} = 10Dr$ yields $Pe_j \sim 6 \times 10^{-2}$.[52] Thus, within the probed range of shear rates, $Pe_j \ll 1$, indicating that the small size of the CNC enables a strong tendency to align under flow and suppresses periodic tumbling. Along the elongation axis of the OSCER, the CNC aligns parallel to the flow, with an orientation of $\langle\theta\rangle \simeq 0°$ to the flow direction. Contrarily, along the compression axis, the CNC align perpendicular to the flow with $\langle\theta\rangle \simeq 90°$. Importantly, $\langle\theta\rangle$ is constant over the whole range of $|\dot{\varepsilon}|$, in agreement with the reported analytical solutions for dilute Brownian suspensions of rodlike particles.[13] Such perpendicular alignment of elongated particles has been previously reported for shear-thinning fluids in the extensional-dominated areas of expansion-flow geometries.[7,19] It is important to note that the fluid advects along the expansion zone of the channel through Poiseuille flow in the case of Newtonian-like fluids and through pluglike flow for shear-thinning fluids, determining different shear rate profiles across the channel width. Due to shear localization at the channel walls, Trebbin et al. showed that shear-thinning fluids generate a larger region of extensionally dominated flow in an expansion-flow geometry than Newtonian fluids.[19] Thus, Trebbin et al. inferred that shear-thinning fluids would cause perpendicular particle alignment over a wider region of the flow geometry than Newtonian fluids.[19] The OSCER geometry in our study has been designed to be "self-lubricating" and to generate a wide region of extensional-dominated and shear-free flow about the primary axes, even for non-shear-thinning or Newtonian fluids.[16,30] Therefore, as the fluid is not sheared along the primary axes of the geometry, the extensional-rheology of the fluid is expected to dominate in this region of the flow geometry.

Solvent Viscosity Scaling. To further clarify the role of the solvent viscosity regarding the different onset of the CNC

https://dx.doi.org/10.1021/acs.macromol.0c02155
Macromolecules 2021, 54, 4176−4185

alignment between the shearing and extensional flows, the CNC was dispersed in an aqueous solution containing 17.2 vol % glycerol (η_s = 1.6 mPa·s). At this glycerol concentration, the relative viscosity (η/η_s) at small deformation rates, is comparable to that of pure water as the solvent fluid, ensuring a negligible change of the hydrodynamic dimensions of the CNC (e.g., possibly due to the compression of the electric double layer), see Figure S4 for the plot of η/η_s vs $\dot{\gamma}$.[27] Due to the higher viscosity, greater deformation rates (thus *Pe*) became accessible for the glycerol mixture compared to pure water, while maintaining a similarly low *Re*. In Figure 6a, the $\langle \Delta n \rangle$ profiles obtained for the SFC and OSCER are compared between the case of water (as shown in Figure 5c) and the 17.2 vol % glycerol mixture as the solvent fluid of the CNC. As expected, the higher viscosity of the glycerol−water mixture causes the increase of $\langle \Delta n \rangle$ to occur at lower deformation rates compared to the case of water as the solvent fluid. Importantly, the shifting of the curves toward lower deformation rates induced by the greater solvent viscosity appears to be analogous to the shift caused by the extensional flow for the same test fluid. In analogy to the water case, the $\langle \Delta n \rangle$ profiles in shearing and pure extension can be superimposed adopting a scaling of $4|\dot{\varepsilon}|$ (Figure 6a, inset). As such, for Newtonian solvents, the onset of alignment in planar extensional flows occurs at a deformation rate 4 times smaller than that for a simple shearing flow due to the solvent extensional viscosity $\eta_{s,E}$ being 4 times greater than η_s (i.e., because $Tr = 4$ for planar elongation). The curves in Figure 6a collapse onto a single master curve when scaled by $Pe = |\dot{\gamma}|/Dr$ for shearing flows and $Pe = |\dot{\varepsilon}|/Dr_E$ for extensional flow, considering $l = l_{max}$ in eqs 1 and 5. For $Pe < 10$, the master curve is well described by a power law fitting with a power law exponent $p = 0.9$, confirming a common trend in the limit of small deformation rates. Moreover, the pronounced rise in $\langle \Delta n \rangle$ occurs at $Pe \simeq 1$, providing an additional indication that the scaling is correct.

Petrie derived analytical solutions, using the Doi−Edwards theory, of *Dr* in the limiting case of small extension rates by accounting for the extensional viscosity of the dispersion, the extensional viscosity of the solvent, and a scaling factor given by *Tr*.[54,55] Importantly, Petrie along with Doi and Edwards, give *Dr* as the scaling diffusion coefficient to determine *Pe* for extensional deformations as $Pe = |\dot{\varepsilon}|/Dr$.[10,54] However, this leads to an underestimation of the *Pe* at which particles align under extensional deformations, specifically at $Pe \simeq 1/4$ instead of $Pe \simeq 1$. The master curve presented in Figure 6b suggests that the onset of CNC alignment can be measured independently from the type of deformation by simply considering the correct solvent viscosity. Therefore, knowing *Dr* and the type of extensional deformation (which sets the value of *Tr*), it is possible to compute the value of $|\dot{\varepsilon}|$ at which the onset of particle alignment should occur ($Pe = 1$) in purely extensional flows as $|\dot{\varepsilon}| = PeDr_E$, which, using eq 5, gives $|\dot{\varepsilon}| = (PeDr)/Tr$. This establishes a straightforward and quantitative relation between shearing and extensional deformations at inducing the alignment of a dilute suspension of rigid rodlike particles. It is however important to note that shearing and extensional flows display remarkably different effects on the particle orientations as measured by the orientation angle $\langle \theta \rangle$ (Figure 5d). For shearing flows, $\langle \theta \rangle$ decreases with increasing shear rate while for extensional flows, $\langle \theta \rangle$ is independent of the rate of deformation. This difference can be directly associated with the absence of the rotational component in the velocity gradient for the elongational flow compared to the shearing flow.

CONCLUSIONS

Combining flow visualization and flow-induced birefringence, we have been able to quantitatively compare the effects of shearing and extensional forces on the alignment of a dilute dispersion of cellulose nanocrystals, consisting of noninteracting negatively charged polydisperse and rodlike rigid particles. Specifically, the ability to perform shear-free extensional deformations within the OSCER microfluidic device enabled the first experimental comparison between shearing and purely extensional flows at aligning colloidal rods in the dilute regime. For Newtonian solvents, the extensional forces are 4 times more effective at inducing particle alignment compared to shear forces. This difference is supported by the different solvent viscosity that the fluid experiences between a shear and extensional region, namely, the shear and extensional solvent viscosity, respectively. From a scaling concept, we show that for a Newtonian solvent, the ratio between extensional viscosity and shear viscosity, namely, the Trouton ratio, determines the different onset of particle alignment between shearing and extensional flows. Specifically, in the limit of small Péclet numbers ($Pe \lesssim 10$), the birefringence signals resulting from the particle alignment in shearing and extensional flows collapse on a single master curve when scaled by a Péclet number that accounts for the solvent shear viscosity and the solvent extensional viscosity, respectively. The proposed scaling unifies the extent of particle alignment between shearing and extensional flows in the limit of small Péclet numbers and gives a straightforward estimation of the alignment of rigid rodlike particles in an extensional flow by knowing the corresponding alignment profile in a shearing flow. This is of particular importance because the extent of alignment in a shearing flow can be easily obtained by several rheo-optical techniques contrarily to the analogous information in a purely extensional flow. In addition, shear and extension rates have displayed a remarkably different effect on particle orientation. In a shear-dominated flow, the particles exhibit a gradual decrease in the orientation angle with increasing shear rate. Contrarily, in the extensional-dominated flow, the particle orientation is deformation-rate-independent and a parallel or perpendicular orientation of the particles to the flow direction is observed along the elongation and compression axes of the geometry, respectively. This is the first experimental report where the effects of shear and pure extensional flows on the alignment of rigid anisotropic particles are quantitatively compared. This understanding will provide the basis to decouple the orientation dynamics in industrially relevant flows, where a combination of shear and extensional rates is usually present and in fluids where interparticle interactions play a crucial role. We envisage that the knowledge provided in this work will help to optimize engineering processes involved with controlled anisotropy. Having demonstrated the influence of the shear and extensional solvent viscosity on controlling the alignment of noninteracting rods for a Newtonian solvent, we aim in future work to broaden this understanding for the more complex non-Newtonian case, using solvent fluids with larger and deformation-rate-dependent Trouton ratios.

https://dx.doi.org/10.1021/acs.macromol.0c02155
Macromolecules 2021, 54, 4176−4185

■ ASSOCIATED CONTENT

Supporting Information

The Supporting Information is available free of charge at https://pubs.acs.org/doi/10.1021/acs.macromol.0c02155.

Profiles of birefringence, Δn, and orientation angle, θ, taken along the x and y axes of the SFC (Figure S1); profiles of Δn and θ profiles taken along the compression and elongation axes of the OSCER (Figure S2); representative AFM image of a drop-cast CNC dispersion at the nanometer length scale (Figure S3); and relative viscosity as a function of the shear rate for the 0.1 wt % CNC in water and the 0.1 wt % CNC in the aqueous glycerol mixture (Figure S4) (PDF)

■ AUTHOR INFORMATION

Corresponding Authors

Vincenzo Calabrese − *Okinawa Institute of Science and Technology, Okinawa 904-0495, Japan;* orcid.org/0000-0001-5974-9217; Email: vincenzo.calabrese@oist.jp

Amy Q. Shen − *Okinawa Institute of Science and Technology, Okinawa 904-0495, Japan;* orcid.org/0000-0002-1222-6264; Email: amy.shen@oist.jp

Author

Simon J. Haward − *Okinawa Institute of Science and Technology, Okinawa 904-0495, Japan;* orcid.org/0000-0002-1884-4100

Complete contact information is available at: https://pubs.acs.org/10.1021/acs.macromol.0c02155

Notes

The authors declare no competing financial interest.

■ ACKNOWLEDGMENTS

The authors gratefully acknowledge the support of Okinawa Institute of Science and Technology Graduate University with subsidy funding from the Cabinet Office, Government of Japan. S.J.H. and A.Q.S. also acknowledge financial support from the Japanese Society for the Promotion of Science (JSPS, Grant Nos. 18K03958 and 18H01135) and the Joint Research Projects (JRPs) supported by the JSPS and the Swiss National Science Foundation (SNSF). The authors thank Dr. Riccardo Funari from the Micro/Bio/Nanofluidics unit at OIST for his assistance with AFM measurements and Dr. Vikram Rathee from the Micro/Bio/Nanofluidics unit at OIST for comments on the manuscript.

■ REFERENCES

(1) Solomon, M. J.; Spicer, P. T. Microstructural regimes of colloidal rod suspensions, gels, and glasses. *Soft Matter* **2010**, *6*, 1391−1400.

(2) Rosén, T.; Hsiao, B. S.; Söderberg, L. D. Elucidating the Opportunities and Challenges for Nanocellulose Spinning. *Adv. Mater.* **2020**, No. 2001238.

(3) Calabrese, V.; da Silva, M. A.; Porcar, L.; Bryant, S. J.; Hossain, K. M. Z.; Scott, J. L.; Edler, K. J. Filler size effect in an attractive fibrillated network: a structural and rheological perspective. *Soft Matter* **2020**, *16*, 3303−3310.

(4) Håkansson, K. M. O.; Fall, A. B.; Lundell, F.; Yu, S.; Krywka, C.; Roth, S. V.; Santoro, G.; Kvick, M.; Prahl Wittberg, L.; Wågberg, L.; Söderberg, L. D. Hydrodynamic alignment and assembly of nanofibrils resulting in strong cellulose filaments. *Nat. Commun.* **2014**, *5*, No. 4018.

(5) Nechyporchuk, O.; Håkansson, K. M. O.; Gowda, V. K.; Lundell, F.; Hagström, B.; Köhnke, T. Continuous assembly of cellulose nanofibrils and nanocrystals into strong macrofibers through microfluidic spinning. *Adv. Mater. Technol.* **2018**, *4*, No. 1800557.

(6) Liu, D.; Wang, S.; Ma, Z.; Tian, D.; Gu, M.; Lin, F. Structure-color mechanism of iridescent cellulose nanocrystal films. *RSC Adv.* **2014**, *4*, 39322−39331.

(7) Kiriya, D.; Kawano, R.; Onoe, H.; Takeuchi, S. Microfluidic control of the internal morphology in nanofiber-based macroscopic cables. *Angew. Chem., Int. Ed.* **2012**, *51*, 7942−7947.

(8) Xin, G.; Zhu, W.; Deng, Y.; Cheng, J.; Zhang, L. T.; Chung, A. J.; De, S.; Lian, J. Microfluidics-enabled orientation and microstructure control of macroscopic graphene fibres. *Nat. Nanotechnol.* **2019**, *14*, 168−175.

(9) De France, K. J.; Yager, K. G.; Chan, K. J. W.; Corbett, B.; Cranston, E. D.; Hoare, T. Injectable anisotropic nanocomposite hydrogels direct in situ growth and alignment of myotubes. *Nano Lett.* **2017**, *17*, 6487−6495.

(10) Doi, M.; Edwards, S. F. *The Theory of Polymer Dynamics*; Oxford University Press, 1986; pp 289−323.

(11) Doi, M.; Edwards, S. F. Dynamics of rod-like macromolecules in concentrated solution Part 1. *J. Chem. Soc., Faraday Trans. 2* **1978**, *74*, 560−570.

(12) Vermant, J.; Yang, H.; Fuller, G. G. Rheooptical determination of aspect ratio and polydispersity of nonspherical particles. *AIChE J.* **2001**, *47*, 790−798.

(13) Dhont, J. K. G.; Briels, W. J. *Soft Matter*; Wiley-VCH: Weinheim, Germany, 2007; Vol. 2, pp 216−283.

(14) Reddy, N. K.; Natale, G.; Prud'homme, R. K.; Vermant, J. Rheo-optical analysis of functionalized graphene suspensions. *Langmuir* **2018**, *34*, 7844−7851.

(15) Winkler, R. G.; Mussawisade, K.; Ripoll, M.; Gompper, G. Rod-like colloids and polymers in shear flow: a multi-particle-collision dynamics study. *J. Phys.: Condens. Matter* **2004**, *16*, 3941−3954.

(16) Haward, S. J.; McKinley, G. H.; Shen, A. Q. Elastic instabilities in planar elongational flow of monodisperse polymer solutions. *Sci. Rep.* **2016**, *6*, No. 33029.

(17) Lang, C.; Hendricks, J.; Zhang, Z.; Reddy, N. K.; Rothstein, J. P.; Lettinga, M. P.; Vermant, J.; Clasen, C. Effects of particle stiffness on the extensional rheology of model rod-like nanoparticle suspensions. *Soft Matter* **2019**, *15*, 833−841.

(18) Oliveira, M. S.; Alves, M. A.; Pinho, F. T.; McKinley, G. H. Viscous flow through microfabricated hyperbolic contractions. *Exp. Fluids* **2007**, *43*, 437−451.

(19) Trebbin, M.; Steinhauser, D.; Perlich, J.; Buffet, A.; Roth, S. V.; Zimmermann, W.; Thiele, J.; Förster, S. Anisotropic particles align perpendicular to the flow direction in narrow microchannels. *Proc. Natl. Acad. Sci. U.S.A.* **2013**, *110*, 6706−6711.

(20) Qazi, S. J. S.; Rennie, A. R.; Tucker, I.; Penfold, J.; Grillo, I. Alignment of dispersions of plate-like colloidal particles of $Ni(OH)_2$ induced by elongational flow. *J. Phys. Chem. B* **2011**, *115*, 3271−3280.

(21) Pignon, F.; Magnin, A.; Piau, J.-M.; Fuller, G. G. The orientation dynamics of rigid rod suspensions under extensional flow. *J. Rheol.* **2003**, *47*, 371−388.

(22) Corona, P. T.; Ruocco, N.; Weigandt, K. M.; Leal, L. G.; Helgeson, M. E. Probing flow-induced nanostructure of complex fluids in arbitrary 2D flows using a fluidic four-roll mill (FFoRM). *Sci. Rep.* **2018**, *8*, No. 15559.

(23) Rosén, T.; Mittal, N.; Roth, S. V.; Zhang, P.; Lundell, F.; Söderberg, L. D. Flow fields control nanostructural organization in semiflexible networks. *Soft Matter* **2020**, *16*, 5439−5449.

(24) Hasegawa, H.; Horikawa, Y.; Shikata, T. Cellulose Nanocrystals as a Model Substance for Rigid Rod Particle Suspension Rheology. *Macromolecules* **2020**, *53*, 2677−2685.

(25) Cheng, N.-S. Formula for the Viscosity of a Glycerol Water Mixture. *Ind. Eng. Chem. Res.* **2008**, *47*, 3285−3288.

(26) Bertsch, P.; Sánchez-Ferrer, A.; Bagnani, M.; Isabettini, S.; Kohlbrecher, J.; Mezzenga, R.; Fischer, P. Ion-induced formation of

nanocrystalline cellulose colloidal glasses containing nematic domains. *Langmuir* **2019**, *35*, 4117−4124.
(27) Bertsch, P.; Isabettini, S.; Fischer, P. Ion-induced hydrogel formation and nematic ordering of nanocrystalline cellulose suspensions. *Biomacromolecules* **2017**, *18*, 4060−4066.
(28) Reid, M. S.; Villalobos, M.; Cranston, E. D. Benchmarking cellulose nanocrystals: From the laboratory to industrial production. *Langmuir* **2017**, *33*, 1583−1598.
(29) Usov, I.; Mezzenga, R. FiberApp: An open-source software for tracking and analyzing polymers, filaments, biomacromolecules, and fibrous objects. *Macromolecules* **2015**, *48*, 1269−1280.
(30) Haward, S. J.; Oliveira, M. S. N.; Alves, M. A.; McKinley, G. H. Optimized Cross-Slot Flow Geometry for Microfluidic Extensional Rheometry. *Phys. Rev. Lett.* **2012**, *109*, No. 128301.
(31) Burshtein, N.; Chan, S. T.; Toda-Peters, K.; Shen, A. Q.; Haward, S. J. 3D-printed glass microfluidics for fluid dynamics and rheology. *Curr. Opin. Colloid Interface Sci.* **2019**, *43*, 1−14.
(32) Haward, S. J.; Kitajima, N.; Toda-Peters, K.; Takahashi, T.; Shen, A. Q. Flow of wormlike micellar solutions around microfluidic cylinders with high aspect ratio and low blockage ratio. *Soft Matter* **2019**, *15*, 1927−1941.
(33) Meinhart, C. D.; Wereley, S.; Gray, M. Volume illumination for two-dimensional particle image velocimetry. *Meas. Sci. Technol.* **2000**, *11*, 809−814.
(34) Wagner, R.; Raman, A.; Moon, R. J. In *Transverse Elasticity of Cellulose Nanocrystals via Atomic Force Microscopy*, 10th International Conference on Wood & Biofiber Plastic Composites, 2010; pp 309−316.
(35) Lang, C.; Kohlbrecher, J.; Porcar, L.; Radulescu, A.; Sellinghoff, K.; Dhont, J. K. G.; Lettinga, M. P. Microstructural understanding of the length- and stiffness-dependent shear thinning in semidilute colloidal rods. *Macromolecules* **2019**, *52*, 9604−9612.
(36) Usov, I.; Nyström, G.; Adamcik, J.; Handschin, S.; Schütz, C.; Fall, A.; Bergström, L.; Mezzenga, R. Understanding nanocellulose chirality and structure−properties relationship at the single fibril level. *Nat. Commun.* **2015**, *6*, No. 7564.
(37) Lang, C.; Lettinga, M. P. Shear flow behavior of bidisperse rodlike colloids. *Macromolecules* **2020**, *53*, 2662−2668.
(38) Tanaka, R.; Saito, T.; Ishii, D.; Isogai, A. Determination of nanocellulose fibril length by shear viscosity measurement. *Cellulose* **2014**, *21*, 1581−1589.
(39) Kobayashi, H.; Yamamoto, R. Reentrant transition in the shear viscosity of dilute rigid-rod dispersions. *Phys. Rev. E* **2011**, *84*, No. 051404.
(40) Lang, C.; Kohlbrecher, J.; Porcar, L.; Lettinga, M. The Connection between Biaxial Orientation and Shear Thinning for Quasi-Ideal Rods. *Polymers* **2016**, *8*, No. 291.
(41) Xu, Y.; Atrens, A.; Stokes, J. R. A review of nanocrystalline cellulose suspensions: Rheology, liquid crystal ordering and colloidal phase behaviour. *Adv. Colloid Interface Sci.* **2020**, *275*, No. 102076.
(42) Shah, R.; London, A. *Laminar Flow Forced Convection in Ducts: a Source Book for Compact Heat Exchanger Analytical Data*; Hartnett, T. I. J. P., Ed.; Academic Press: New York, 1978.
(43) Haward, S. J. Microfluidic extensional rheometry using stagnation point flow. *Biomicrofluidics* **2016**, *10*, No. 043401.
(44) Haward, S. J.; Jaishankar, A.; Oliveira, M. S. N.; Alves, M. A.; McKinley, G. H. Extensional flow of hyaluronic acid solutions in an optimized microfluidic cross-slot device. *Biomicrofluidics* **2013**, *7*, No. 044108.
(45) Macosko, C. W. Rheology Principles. In *Measurements, and Applications*; VCH Publishes, 1994; pp 285−335.
(46) Macosko, C. W. Rheology Principles. In *Measurements, and Applications*; VCH Publishes, 1994; pp 65−108.
(47) Trouton, F. T. On the coefficient of viscous traction and its relation to that of viscosity. *Proc. R. Soc. London, Ser. A* **1906**, *77*, 426−440.
(48) Petrie, C. J. Extensional viscosity: A critical discussion. *J. Non-Newtonian Fluid Mech.* **2006**, *137*, 15−23.
(49) Sun, C.-L.; Huang, H.-Y. Measurements of flow-induced birefringence in microfluidics. *Biomicrofluidics* **2016**, *10*, No. 011903.
(50) Rosén, T.; Wang, R.; Zhan, C.; He, H.; Chodankar, S.; Hsiao, B. S. Cellulose nanofibrils and nanocrystals in confined flow: Single-particle dynamics to collective alignment revealed through scanning small-angle X-ray scattering and numerical simulations. *Phys. Rev. E* **2020**, *101*, No. 032610.
(51) Singh, A. P.; Rey, A. D. Computer simulation of dynamics and morphology of discotic mesophases in extensional flows. *Liq. Cryst.* **1995**, *18*, 219−230.
(52) Zöttl, A.; Klop, K. E.; Balin, A. K.; Gao, Y.; Yeomans, J. M.; Aarts, D. G. Dynamics of individual Brownian rods in a microchannel flow. *Soft Matter* **2019**, *15*, 5810−5814.
(53) Petrie, C. J. The rheology of fibre suspensions. *J. Non-Newtonian Fluid Mech.* **1999**, *87*, 369−402.
(54) Petrie, C. J. Some asymptotic results for planar extension. *J. Non-Newtonian Fluid Mech.* **1990**, *34*, 37−62.
(55) Petrie gives in the limit of small rate of deformations: $Dr = \frac{\nu k_B T}{(\eta_p) - (T\eta_s)} \frac{2}{3}$ for planar extension and $Dr = \frac{\nu k_B T}{(\eta_u) - (T\eta_s)} \frac{1}{2}$ for uniaxial extension, where η_p is the planar extensional viscosity and η_u is the uniaxial extensional viscosity. For small rate of deformations $\eta_p = T\eta_0$ and $\eta_u = T\eta_0$, yielding a generalized form as $\frac{Dr}{Tr} = \frac{\nu k_B T}{(T\eta_0) - (T\eta_s)} \frac{1}{6}$

https://dx.doi.org/10.1021/acs.macromol.0c02155
Macromolecules 2021, 54, 4176−4185